Field evaluation of broadband spectral electrical imaging for soil and aquifer

characterization

M. Kelter<sup>(1)</sup>, J.A. Huisman<sup>(1)</sup>, E. Zimmermann<sup>(2)</sup>, and H. Vereecken<sup>(1)</sup>

5

10

(1) Agrosphere (IBG 3), Institute of Bio- and Geosciences, Forschungszentrum Jülich GmbH,

52425 Jülich, Germany.

(2) Electronic Systems (ZEA 2), Central Institute of Engineering, Electronics and Analytics,

Forschungszentrum Jülich GmbH, 52425 Jülich, Germany

(3) Department of Geodynamics and Geophysics, University of Bonn, 53115 Germany.

15

Corresponding Author: s.huisman@fz-juelich.de

Tel. +49 246161 8607

20 **Postprint of:** 

Kelter, M., J.A. Huisman, E. Zimmermann, and H. Vereecken. 2018. Field evaluation of

broadband spectral electrical imaging for soil and aquifer characterization. Journal of Applied

Geophysics, 159, 484-496. https://doi.org/10.1016/j.jappgeo.2018.09.029.

25

#### Abstract

30

35

40

Spectral electrical impedance tomography (EIT) involves the imaging of the complex electrical distribution in the mHz to kHz range. Until now, field EIT measurements were limited to frequencies below 100 Hz because strong electromagnetic coupling effects associated with longer cables and high electrode contact impedances prohibit accurate field measurements at higher frequencies. In this paper, we aim to evaluate the capability of recent improvements in the pre-processing and inversion of wideband EIT measurements to improve the accuracy and spectral consistency of field EIT measurements of the complex electrical conductivity distributions in the mHz to kHz frequency range. In a first case study, time-lapse surface EIT measurements were performed during an infiltration experiment to investigate the spectral complex electrical conductivity as a function of water content. State-of-the-art data processing and inversion approaches were used to obtain images of the complex electrical conductivity in a frequency range from 100 mHz to 1 kHz, and integral parameters were obtained using Debye decomposition. Results showed consistent spectral and spatial variation of the phase of the complex electrical conductivity in a broad frequency range, and a complex dependence on water saturation. In a second case study, borehole EIT measurements were made in a well-characterized gravel aquifer. These measurements were inverted to obtain broadband images of the complex conductivity after correction of inductive coupling effects using a recently developed correction procedure that relies on a combination of calibration measurements and model-based corrections. The inversion results were spatially and spectrally consistent in a broad frequency range up to 1 kHz only after removal of inductive coupling effects. Overall, it was concluded that recent improvements in spectral EIT measurement technology combined with advances in inversion and data processing now allow accurate broadband EIT measurements up to 1 kHz.

50

#### 1. Introduction

55

60

65

70

75

Spectral electrical impedance tomography (EIT) is a geophysical imaging method that provides the distribution of the complex electrical conductivity in the mHz to kHz frequency range (Slater 2007; Kemna et al., 2012; Revil et al., 2012). Whereas the real part of the complex electrical conductivity is determined by ionic conduction in the pore space, the imaginary part of the complex electrical conductivity is determined by polarization processes associated with the electrical double layer at the interface between the soil matrix and the pore fluid (Börner et al. 1996; Revil and Florsch, 2010). In recent years, there has been increasing interest in the use of EIT for a range of environmental engineering applications (Kemna et al., 2000, 2004) with a particular focus on contaminated site investigations (e.g. Williams et al., 2009; Flores-Orozco et al., 2012b). Such field investigations have been fueled by a range of laboratory investigations with spectral induced polarization (SIP) measurements that have provided mechanistic understanding of the polarization processes that determine the complex electrical conductivity (Titov et al., 2002, 2004; Revil and Florsch, 2010; Bücker and Hördt, 2013). These laboratory SIP investigations have also shown that the complex electrical conductivity exhibits a characteristic frequency dependence that depends on the involved polarization length scales within the subsurface (e.g. Leroy et al., 2008; Bairlein et al., 2014). Therefore, there is considerable interest to obtain field measurements of the complex electrical conductivity in the in the mHz to kHz frequency range.

Despite continuous progress in the development of EIT inversion codes and strategies (Oldenburg and Li, 1994; Kemna, 2000; Flores-Orozco et al., 2012a) as well as recent improvements in the analysis of spectral inversion results (Kelter et al., 2015; Weigand and Kemna, 2016), it is still challenging to make accurate EIT measurements of the complex electrical conductivity in the field, especially for frequencies above 50 Hz. Depending on the type of application, there may be different reasons for this reduced accuracy. In the case of

borehole or surface EIT measurements with long cables, many applications have been limited to frequencies below 10 Hz (e.g. Flores-Orozco et al., 2011) due to electromagnetic coupling effects. Especially inductive coupling between the electrical wires used for current injection and potential measurements strongly affects impedance measurements when long multicore cables are used (e.g. Pelton et al., 1978). In order to account for such inductive coupling effects on spectral EIT measurements, Zhao et al. (2013, 2015) developed a correction method that relies on a combination of calibration measurements and numerical modelling of the cable layout. The use of this correction method significantly improved the data quality for higher frequencies to an accuracy of about 1 mrad for frequencies up to 1 kHz for EIT measurements in water. However, an extensive field evaluation of these novel correction procedures has not been performed yet.

Another application where field EIT measurements in a broad frequency range are challenging is the investigation of vadose zone processes. Several studies investigated the relationship between spectral electrical parameters and water content in the laboratory (Ulrich and Slater, 2004; Binley et al., 2005; Breede et al., 2011; Kelter et al., 2015), but only Ghorbani et al. (2008) presented an in-situ investigation of the effect of changes in soil water content on the measured phase shift. They found that an increase in water content resulted in an increase in the phase shift of the complex electrical conductivity below 100 Hz, whereas a decrease in phase shift was observed above 100 Hz. A common problem for accurate phase measurements in the Hz to kHz frequency range for vadose zone applications is the electrode contact impedance, which increases drastically for dry soil (Breede et al., 2011; Huisman et al., 2015; Kelter et al., 2015). An approach to correct electrical impedance measurements for the effect of electrode contact impedances was proposed in Huisman et al. (2016) for laboratory SIP measurements and in Kelter et al. (2015) for laboratory EIT measurements. In the latter study with very dry soil, the use of this correction extended the interpretable

frequency range up to 200 Hz. However, the value of such correction strategies to account for the effects of electrode contact impedances has not been evaluated in the field, where contact impedances are much more difficult to control and also depend strongly on the selected electrode type.

In this paper, we aim to evaluate the capability of recent improvements in the pre-processing and inversion of wideband EIT measurements to improve the accuracy and spectral consistency of field EIT measurements of the complex electrical conductivity distributions in the mHz to kHz frequency range using two case studies. The first case study deals with an irrigation experiment on an initially dry soil, where spectral electrical measurements were performed in a frequency range from 0.1 Hz up to 1 kHz using surface electrodes. EIT measurements were made before, during, and after irrigation in order to investigate the relation between water content and the inverted spectral electrical conductivity distributions. Two electrodes types were used in this case study and their performance was compared based on measurement accuracy using normal-reciprocal analysis. The second case study deals with borehole EIT measurements using long multicore cables in a well characterized aquifer at the Krauthausen test site (e.g. Vereecken et al., 2000; Hördt et al., 2007; Müller et al., 2010). In both case studies, spectral electrical parameters were estimated using a Debye-decomposition approach and the obtained spatial distributions of the spectral electrical parameters were evaluated using ground truth data.

# 2. Materials and Methods

105

110

115

120

125

#### 2.1. Measurement principle and system

In order to perform measurements of the spectral complex electrical impedances in the field, an EIT system similar to the one described in Zimmermann et al. (2008a) was used. The EIT system has 40 channels and was modified in such a way that reciprocal measurements (i.e.

switching of current and voltage dipoles) are possible. This was achieved by using so called electrode modules that consist of an internal relay for current injection and an amplifier for potential measurements. These modules are connected directly to the electrodes. Connection to the data acquisition channels of the system is achieved with shielded twisted pair cables of 5 m length in the irrigation experiment. In case of the borehole measurements, the modules were connected to an adapter box very close to the measurement system using a 25 m long multicore cable that was composed of 16 shielded, twisted wire pairs. Potential measurements are performed relative to system ground, which enables the a posteriori calculation of arbitrary voltage dipole pairs for a given current injection.



140 Figure 1: Photograph of the measurement setup of the irrigation experiment showing the two used electrode profiles of non-polarizable (left profile) and stainless steel (right profile) electrodes. Also shown are the access trench at the beginning of the profile and the drip tube system that was used for irrigation.

# 2.2. Site description and experimental setup

130

# 145 2.2.1. Irrigation experiment

150

155

160

170

The first case study presents an irrigation experiment on initially dry soil. For this, a roofed plot of 7 m length and 3 m width with a drip irrigation system was used. The plot is part of the field rhizotron facility described in detail in Cai et al. (2016). The soil is characterized by a very high gravel content of 40%, and the fine fraction has a silt loam texture with 23% sand, 63% silt and 14% clay (Vanderborght et al., 2010). An overview of the general set-up of the irrigation experiment is provided in Figure 1. One side of irrigated plot is bordered by a trench, which was excavated in order to install additional sensors. In particular, hourly Time Domain Reflectometry (TDR) measurements were made using a TDR100 system (Campbell Scientific, Logan, USA) with custom-made three-wire probes with a length of 20 cm. Four TDR probes each were installed in six depths (10, 20, 40, 60, 80, and 120 cm), and the mean of the four sensors at each depth is used in this study. In order to convert the dielectric permittivity  $\varepsilon$  measured with TDR to water content  $\theta$ , a calibration relationship was determined in the laboratory. For this, air-dried soil from different soil layers was mixed with a known amount of water and packed to the same bulk density as the field soil. TDR measurements were used to determine the permittivity of these packed samples with a known water content. It was found that the resulting site-specific calibration relationships were similar for the different soil layers. Therefore, the following relationship was used to estimate soil water content from permittivity for all soil layers:

$$\theta = 0.1045 \cdot \sqrt{\varepsilon} - 0.1671. \tag{1}$$

For more information on the calibration of TDR, the reader is referred to Cai et al. (2016).

A drip irrigation system was used for five applications of water that lasted 90 minutes each and a sixth irrigation which lasted about 55 minutes. The plot was homogeneously irrigated to the extent possible by using a distance of 30 cm between individual drippers and a separation of 30 cm between each tube with drippers. Table 1 provides details about start and end time of

all irrigation events together with information about the electrical conductivity and temperature of the irrigation water. The fifth irrigation event was started directly after the fourth event in order to perform measurements during stationary flow conditions.

175 Table 1. Irrigation schedule and information about irrigation water.

180

185

190

	Infiltration 1	Infiltration 2	Infiltration 3	Infiltration 4	Infiltration 5	Infiltration 6
Start Time	20130930	20131001	20131002	20131003	20131003	20131004
	14:54	12:27	12:45	12:24	14:28	09:45*
End Time	20130930	20131001	20131002	20131003	20131003	20131004
	16:24	13:57	14:15	13:54	15:58	10:40
Amount (dm <sup>3</sup> )	597	573	587	548	566	360
Amount (mm)	28.4	27.3	28	26.1	27	17.1
T (°C)	17	17	16	14.4	14.4	14.4*
EC (µS/cm)	513	513	500	488	488	488*

<sup>\*</sup> Event was started accidently. Start time has been estimated from known amount of irrigated water and mean application rate of infiltration event 1-5. Values for temperature and electrical conductivity were taken from previous date.

Two types of electrode arrays were used for the infiltration experiment (Figure 1). The first electrode array consisted of 28 non-polarizable Cu/CuSo4 electrodes (model 3-A "Fat Boy", Tinker & Rasor, San Bernardino, CA, USA) with an electrode spacing of 0.25 m and a ceramic plate diameter of 6 cm. Wetted sponges were used to obtain a homogeneous contact between the ceramic plate and the uneven soil surface. This type of electrode has the advantage that they do not need to be inserted into the soil. Furthermore, the overvoltage of electrodes that have already been used for current injection decays much faster compared to the more widely used stainless steel electrodes (Kemna et al., 2012). In addition, this electrode type provides a large contact area to the soil surface, which results in relatively low electrode contact impedances. This is beneficial for accurate EIT measurement in the kHz frequency range (Huisman et al., 2016).

The second electrode array consisted of 40 stainless steel electrodes with an electrode spacing of 18 cm and was installed in parallel to the electrode array of non-polarizable electrodes with a separation of 1 m in order to compare the performance of the two electrode types. The steel electrodes had a length of 10 cm and a diameter of 1 cm and were inserted by at least 2 cm into to soil to ensure sufficient contact. In the case of the non-polarizable electrodes, the length of the cables to connect the electrodes to the EIT system was 5 m, whereas it was 8 m in case of the steel electrodes. The use of such short cables with sufficient separation avoids the need to correct for inductive coupling between the cables, as it is also done in laboratory EIT measurements (Zimmermann et al., 2008a; Kelter et al., 2015).

A combination of skip-0, skip-2 and skip-8 current injection configurations (e.g. current injection at electrodes 1-2; 1-4 and 1-10, respectively) was used for data acquisition. All possible pairs of voltage dipoles with the same skips were calculated a posteriori for each current injection in order to have a full set of normal and reciprocal measurements. For the electrode array with non-polarizable electrodes, the total number of normal and reciprocal measurement configurations was 6128, whereas 13080 normal and reciprocal measurement configurations were obtained for the array of stainless steel electrodes. Spectral measurements were only made using the non-polarizable electrodes at 14 frequencies equally spaced in logarithmic space from 0.1 Hz to 1 kHz. The data acquisition time was 100 minutes for a full set of spectral EIT measurements with non-polarizable electrodes and 10 minutes for a single frequency EIT measurement at 2.5 Hz using the stainless steel electrodes. In order to correct for the effect of high contact impedances on the EIT measurements, the correction procedure outlined in Kelter et al. (2015) was used.

#### 2.2.2. Borehole EIT measurements in a well characterized aquifer

The second case study deals with EIT borehole measurements in the well characterized heterogeneous unconfined aquifer of the Krauthausen test site (see e.g. Vereecken et al., 2000; Hördt et al., 2007; Müller et al., 2010). This test site is located approximately 10 km northwest of the city of Düren and about 6 km from the Forschungszentrum Jülich, Germany. The base of the aquifer is located at a depth of 11 to 13 meter and consists of intermitting layers of clay and silt. The upper part of the aquifer is divided into 3 layers with the Rur sediments at the top, followed by the upper and lower Rhine sediments. Heterogeneity in the upper part is mostly related to differences in gravel content (Vereecken et al., 2000). A detailed description of the Krauthausen test site can be found in Vereecken et al. (2000) and Tillmann et al. (2007).

Borehole EIT measurements were made using two custom-made active electrode chains each consisting of eight electrodes with a separation of 1 m. Brass ring electrodes with a diameter of 42 mm and a height of 10 mm were used. More details about these active electrode chains can be found in Zhao et al. (2013) and Zhao et al. (2015). EIT measurements were performed in two boreholes (B75 and B76) that were separated by 5 m. Electrodes in borehole B75 were numbered from 1 to 8, and electrodes in borehole B76 were numbered from 9 to 16. The current injection consisted of skip-0 (1-2, 2-3, ...., 9-10,...), skip-2 (1-4, 2-5, ..., 9-12, ...), skip-4, skip-5, skip-6 in each of the two boreholes, and cross-hole (skip-8) configurations (1-9, 2-10, ...). In post-processing, all possible pairs of voltage dipoles with the same skips were calculated for each current injection in order to have a full set of normal and reciprocal measurements. Therefore, the total number of normal and reciprocal measurement configurations was 3000. Spectral measurements were made at 18 frequencies equally spaced in logarithmic space from 1.6 Hz to 3.15 kHz. Each current injection was repeated with switched polarity to correct the injected current (see Zimmermann et al., 2008a). This

procedure to obtain a more accurate estimate of the injected current is time-consuming because all measurements need to be taken twice. Therefore, it was not considered in the first case study where time was considered to be a limiting factor in survey design. The data acquisition time was 110 minutes for a full set of spectral EIT measurements in this second case study. During installation of the boreholes B75 and B76, sediment was collected during drilling. The gravel, sand, silt and clay content of this sample material was determined and this information will be used to validate the field EIT measurements.

245

250

255

260

265

Calibration measurements and numerical modelling of the layout of the electrode chains were used in order to correct for inductive coupling effects between cables following the procedures outlined in Zhao et al. (2013, 2015). In this correction procedure, the measured impedances *Z* are described by

$$Z = Z_{Soil} + i\omega M, \tag{2}$$

where  $Z_{Soil}$  is the impedance of the soil and  $i\omega M$  is the inductive coupling between the cables that needs to be removed. M is the mutual inductance of the corresponding measurement configuration. The mutual inductances of all possible two-wire pairs in one borehole chain or between two borehole chains are put into four submatrices, which results in the following pole-pole matrix

$$M = \begin{bmatrix} M_1 & M_{12} \\ M_{21} & M_2 \end{bmatrix}, \tag{3}$$

where the diagonal submatrices  $M_1$  and  $M_2$  define the mutual inductances between wire pairs in chain 1 and 2, respectively, and  $M_{21}$  and  $M_{12}$  define the mutual inductances between wire pairs in the two separate chains. The mutual inductances in  $M_1$  and  $M_2$  were determined using calibration measurements (Zhao et al., 2015). The mutual inductances in  $M_{12}$  and  $M_{21}$  were obtained by a numerical solution of the Neumann-integral in MATLAB for a particular set of wire pairs (see e.g. Jackson, 1975):

$$M = \frac{\mu}{4\pi} \int_{C_1}^{C_2} \int_{P_1}^{P_2} \frac{d\vec{s}d\vec{S}}{r},\tag{4}$$

where *s* and *S* are infinitesimal wire segments of current and potential wires, C<sub>1</sub>, C<sub>2</sub>, P<sub>1</sub> and P<sub>2</sub> are the start and end positions of wires for current injection and potential measurement, respectively, and *r* is the distance between the two wires. In order to use this correction procedure, the layout geometry of the electrical cable needs to be known with cm accuracy. This was achieved by using the simple cable geometry shown in Figure 2. For more details about the calibration measurements and the calculation of the mutual inductance, the reader is referred to Zhao et al. (2015).

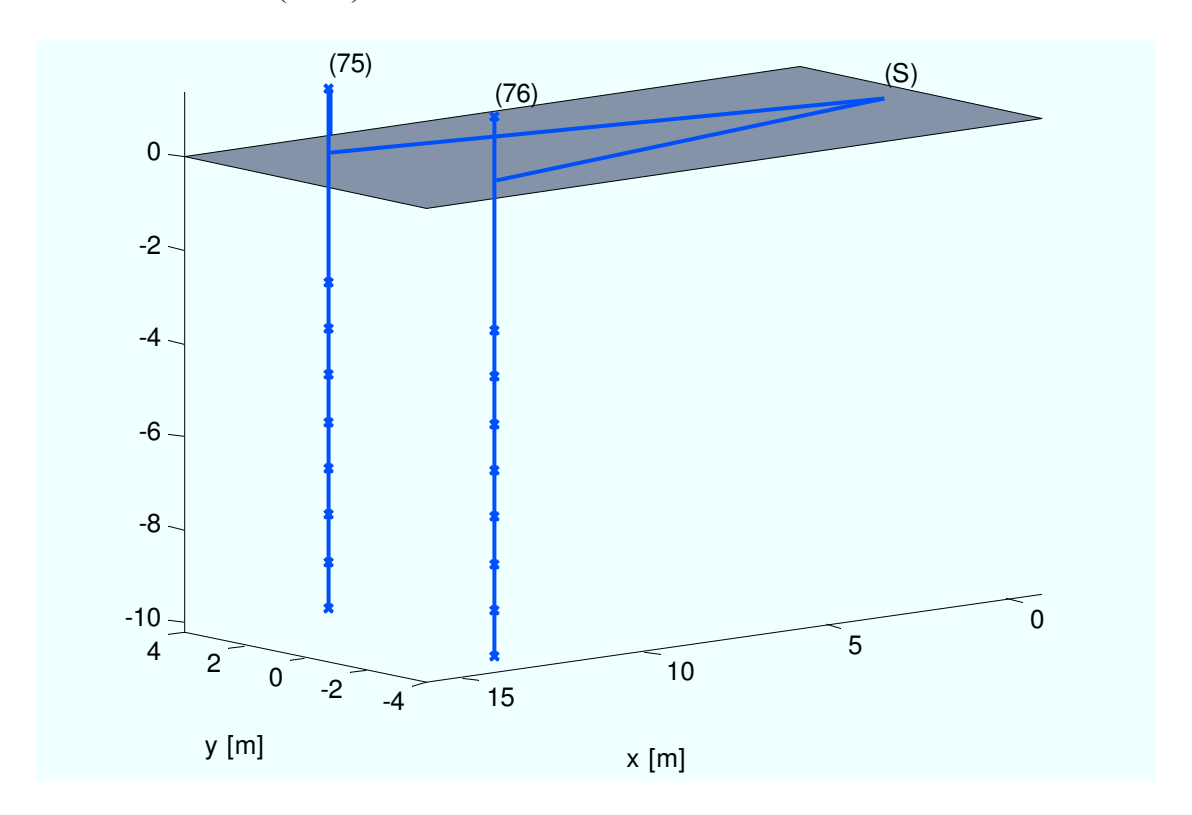


Figure 2. Cable layout (blue line) of the borehole EIT measurements with the measurement system (S) at location (0.00, 0.00), borehole 75 at location (13.20, 2.50), and borehole 76 at location (12.80, -2.40).

# 285 2.3. Inversion methodology

Inversion of the EIT data obtained in both case studies was done using the 2.5 D inversion code CRTomo developed by Kemna (2000). This code uses log-transformed magnitude and phase shift as data, and iteratively minimizes the objective function:

$$\Psi(\mathbf{m}) = \|\mathbf{W}_d[\mathbf{d} - \mathbf{f}(\mathbf{m})]\|^2 + \lambda \|\mathbf{W}_m \mathbf{m}\|^2, \tag{5}$$

where  $\mathbf{d}$  is the complex valued data vector,  $\mathbf{m}$  is the model vector of complex electrical conductivities,  $\mathbf{f}(\mathbf{m})$  is the vector of the forward response of model  $\mathbf{m}$ ,  $\lambda$  is the regularization parameter, and  $\mathbf{W}_d$  and  $\mathbf{W}_m$  are the data weighting and model roughness matrix, respectively. Because of the ill-posedness of this inverse problem, some sort of regularization is needed in order to achieve a unique and stable solution. Here,  $\mathbf{W}_m$  represents a first-order roughness operator that is used to penalize overly rough models during inversion. When the subsurface is known to be layered, an anisotropic smoothing factor is often used to define  $\mathbf{W}_m$  in order to strengthen smoothing in horizontal direction (Kemna, 2000). In the second case study with borehole EIT data, we used an anisotropic smoothing factor of 50 based on experience from previous studies and trial and error to obtain the expected layered inversion results.

300

305

290

295

The entries of the data weighting matrix  $\mathbf{W}_d$  were derived from the inverse of the individual data errors, which were estimated from the analysis of normal and reciprocal measurements using a so-called multi-bin approach (see e.g. Koestel et al., 2008; Flores-Orozco et al., 2012a). This analysis provided error parameters for the magnitude and the phase of the measured electrical impedances for each individual frequency. In this multi-bin approach, the data are binned according to the measured magnitude. Then, the standard deviation of the discrepancies between normal and reciprocal measurements inside each bin is calculated for the magnitude and phase. Finally, error models are fitted to these standard deviations as a function of the mean measured magnitude. In this study, the selected error model for the magnitude of the electrical conductivity was:

310 magn

$$\varepsilon_{mag} = a_{mag} + b_{mag} \cdot |Z|,\tag{6}$$

where  $a_{mag}$  represents the absolute measurement error and  $b_{mag}$  represents the relative measurement error. The error model for the phase was defined as:

$$\varepsilon_{pha} = a_{pha} |Z|^{-b_{pha}},\tag{7}$$

where  $a_{pha}$  and  $b_{pha}$  are fitting parameters of the phase error model. In case of the magnitude, an additional relative modelling error of 3% was added to the estimated relative error parameter in order to account for positional errors of the electrodes as well as the approximation introduced by the use of a 2.5D forward modelling and inversion approach that neglects variations in the conductivity distribution in the strike direction of the electrode profile.

In order to obtain robust estimates of the data error and reasonable data for the inversion, the measured data were filtered prior to further analysis. In a first step, all measurements that showed a standard deviation of three repeated measurements of more than 10% for the real part and 100% for the imaginary part of the complex electrical impedance were removed. Furthermore, measurements were not considered when the difference between normal and reciprocal measurements was higher than two standard deviations of normal-reciprocal differences for both magnitude and phase shift of the whole data set. Finally, measurements with physically implausible positive phase shifts of the complex impedances were removed. In the case of the EIT measurements obtained during the irrigation experiment, an additional filter was used. In particular, unreasonably high negative phase shift values were removed that were mostly caused by the strong polarization associated with the metallic TDR probes on one side of the EIT transect. The threshold value for this filter was empirically estimated for each individual frequency based on the distribution of measured phase shifts and the position of the electrode configuration (i.e. only configurations that were likely affected by

325

330

the presence of the TDR probes were removed). Obviously, the removal of these measurements decreased the coverage within the EIT transect, in particular for the deeper soil layers. However, the resulting inversion results were much better using this additional filter in terms of plausibility and spectral consistency, especially in the low frequency range where polarization caused by the TDR probes was observed to be very high.

After determination of the data weighting matrix and data filtering, the spectral EIT measurements were inverted following the procedures established in Kemna (2000) and Kelter et al. (2015). In summary, the inversion process is started using a homogeneous starting model, a high value of the regularization parameter  $\lambda$ , and a central frequency of 10 Hz. Equation (5) is iteratively minimized by updating the model parameters  $\mathbf{m}$  and the regularization parameter  $\lambda$  until the error-weighted root mean square error (RMSE) reaches a value of 1:

$$RMSE = \frac{1}{\sqrt{N}} \sqrt{\|\mathbf{W}_d(\mathbf{d} - \mathbf{f}(\mathbf{m}))\|^2}$$
 (8)

where N is the number of measurements. Since the complex model error in  $\mathbf{W}_d$  is dominated by  $\varepsilon_{mag}$ , it may occur that the RMSE is already close to 1 while the actual fit to the phase values still is rather poor. In order to overcome this issue, a so-called final phase improvement was performed in both case studies. This is an additional inversion in which the fit to the measured phase values is improved by only varying the modelled phase while keeping the resistivity magnitude fixed. For more details, the reader is referred to Kemna (2000). The resulting inverted model for 10 Hz was then used as a starting model for all other frequencies.

# 2.4. Spectral analysis

340

345

360

A Debye-decomposition approach (Nordsiek and Weller, 2008) was used in order to obtain integral spectral parameters that summarize the spectral response of the complex electrical

conductivity. In this approach, the complex resistivity spectrum  $\rho^*(\omega)$  is decomposed into a superposition of N Debye relaxations:

$$\rho^*(\omega) = \rho_0 \left[ 1 - \sum_{k=1}^{N} m_k \left( 1 - \frac{1}{1 + (i\omega \tau_k)} \right) \right]$$

$$\tag{9}$$

with  $\rho_0$  the DC-resistivity and  $m_k$  the chargeability corresponding to the relaxation time  $\tau_k$ . Integral spectral parameters can be estimated from the resulting chargeability distribution, such as the total chargeability,  $m_{tot}$ 

$$\mathbf{m}_{\text{tot}} = \sum_{k=1}^{N} \mathbf{m}_{k},\tag{10}$$

and the normalized total chargeability  $m_n^{\text{tot}}$ :

365

380

385

$$m_n^{\text{tot}} = \frac{m_{\text{tot}}}{\rho_0},\tag{11}$$

The former is a measure of the total polarizability of the sample and reflects the area under the phase spectrum. The latter was proposed by Weller et al. (2010) as a more robust measure of the IP effect compared to m<sub>tot</sub>, which is independent of changes in the DC resistivity. Characteristic relaxation times can also be obtained from the chargeability-weighted relaxation time distributions. A commonly used characteristic relaxation time (Flores-Orozco et al., 2012b; Kelter et al., 2015; Weigand and Kemna, 2016) is the chargeability-weighted logarithmic mean relaxation time τ<sub>mean</sub>:

$$\tau_{\text{mean}} = \exp(\frac{1}{m_{\text{tot}}} (\sum_{k=1}^{N} m_k \ln(\tau_k))). \tag{12}$$

Alternatively, peak relaxation times (if present) or cumulative relaxation times that represent a threshold relaxation time where a certain percentage of the total chargeability has been reached (i.e.  $\tau_{50}$  for the median) can be used.

The implementation of our Debye-decomposition approach was based on the Tikhonov-regularized optimization scheme described in Zisser et al. (2010), which was modified to allow automated analysis of spectral tomography data. In this approach, the complex electrical resistivity at each frequency for each pixel was collected to obtain the frequency

spectrum of the complex resistivity for each pixel. The time axis was discretized using 100 relaxation times that ranged from  $\frac{1}{(10\cdot 2\pi f_{\text{max}})}$  s to  $\frac{10}{(2\pi f_{\text{min}})}$  s and a first order smoothness-constraint was applied to the chargeability (see e.g. Zisser et al., 2010; Weigand and Kemna, 2016). After this inversion, integral spectral parameters were calculated using the chargeability values corresponding to relaxation times within the measured frequency range only.

# 3. Results and Discussion

390

395

400

405

410

3.1. Irrigation experiment on an initially dry soil

3.1.1. Measurement error analysis and comparison of non-polarizable and steel electrodes Figure 3 shows a comparison of the measurement accuracy with stainless steel and nonpolarizable electrodes in terms of differences between normal and reciprocal measurements for the magnitude (top) and phase shift (bottom) of the measured complex electrical impedance at 2.5 Hz after data filtering. The data were obtained for a wet soil and therefore present a best-case-scenario because of the low electrode contact impedances. The results indicate that the measurement accuracy of the impedance magnitude was similar for the two electrode types for impedance magnitudes ranging from 1 to 250  $\Omega$ . For higher impedance magnitudes obtained for greater dipole lengths (not shown here), the measurement accuracy decreased significantly for the steel electrodes whereas the measurement accuracy of the nonpolarizable electrodes remained relatively constant. Figure 3 also presents the differences between normal and reciprocal measurements for the phase of the impedance. It can be seen that these differences are much smaller for the non-polarizable electrodes over the entire range of measured impedance magnitude (please note different scaling of y-axis). This clearly suggests that a higher measurement accuracy can be achieved with this electrode type as compared to the stainless steel electrodes.

Figure 4 presents the binned data corresponding to Figure 3, and the fitted error model including the associated model parameters. The magnitude of the impedance obtained with non-polarizable electrodes showed a relatively constant measurement error, whereas the measurement error for the stainless-steel electrodes showed a small but significant increase with increasing magnitude of the measured impedance. The absolute error of the impedance magnitude  $b_{mag}$  was similarly low for both electrode types. Compared to previous studies (Bechtold et al., 2012; Kelter et al., 2015), the obtained absolute and relative errors for the steel and non-polarizable electrodes are in a reasonable range.

415

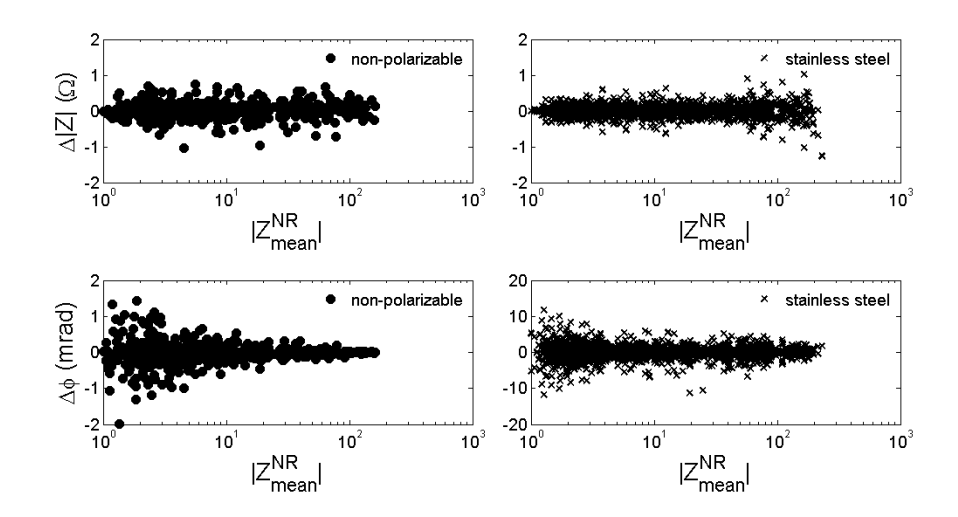


Figure 3. Comparison of differences between normal and reciprocal measurements of the magnitude (top) and phase shift (bottom) of complex electrical impedance measurements at a frequency of 2.5 Hz using non-polarizable (left) and stainless steel electrodes (right).

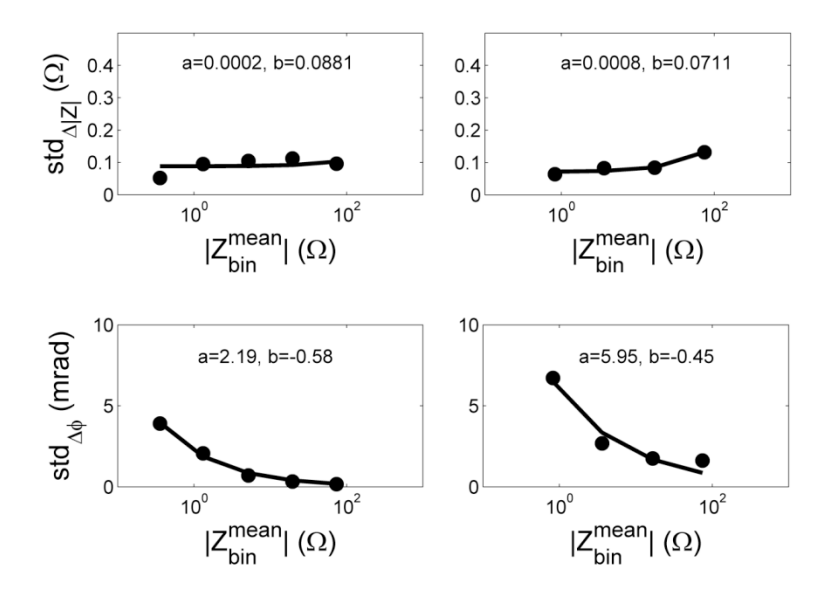


Figure 4. Error models obtained by multi-bin normal-reciprocal analysis of data measured at a frequency of 2.5 Hz using a linear error model for the magnitude data (top) and an inverse power law relationship for the phase shift data (bottom) for non-polarizable Cu/CuSO4 electrodes (left) and stainless steel electrodes (right). The resulting error model parameters are also shown.

For the phase shift, the differences in data quality between the stainless steel and the non-polarizable electrodes were observed to be much larger. Figure 4 shows that measurement errors are substantially higher for the phase of the impedance measured with stainless steel electrodes, especially for low transfer impedances. Most likely, this is due to the stronger effects of systematic errors like polarization of electrodes that have been previously used for current injection before subsequent voltage measurements, as well as inhomogeneous and high contact impedances. The latter explanation is further supported by the even higher measurement errors observed for drier soil conditions when using stainless steel electrodes (not shown). The error parameters for the phase shift obtained with non-polarizing electrodes corresponded well with values observed in Flores-Orozco et al. (2012a), who reported  $a_{pha} = 1.79$  and  $b_{pha} = -0.18$  at a frequency of 0.125 Hz. Because of the higher

measurement accuracy, we will only present results obtained using the non-polarizable electrodes in the following.

Figure 5 presents the development of the error parameters for all spectral measurements performed during the irrigation experiment as a function of frequency. It can be seen that the relative error parameter b<sub>mag</sub> for the magnitude of the complex electrical impedance remains very low and independent of frequency. For instance, the relative error remained below 1 % except for the high frequencies of the first measurement at day 0 (dry soil), as well as for the second set of measurements on day 3 that was obtained during an irrigation event where stationary conditions were assumed but maybe not fully realized. Non-stationarity can introduce systematic difference in the magnitude of the impedance of normal and reciprocal measurements due to actual changes in water content during data acquisition. The absolute model parameter a<sub>mag</sub> of the magnitude of the complex electrical impedance was generally low for all measurement days too, except again for the first measurements in dry soil where the absolute error increased to around 1 Ω.

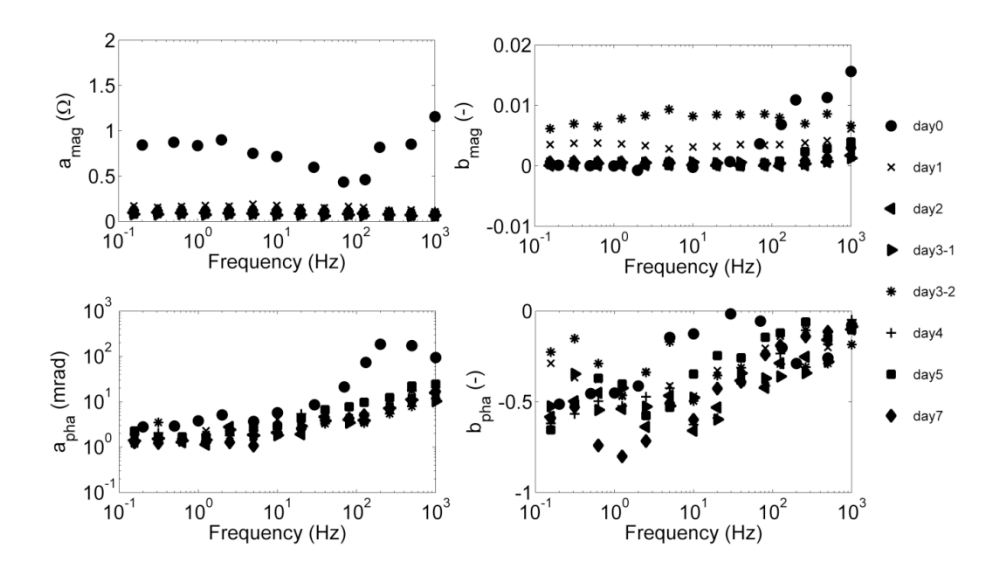


Figure 5. Spectral behaviour and temporal evolution of error parameters for magnitude (top row) and phase shift (bottom row), estimated using normal-reciprocal analysis during the irrigation experiment for measurements using non-polarizable electrodes.

The measurement accuracy of the phase shift varied much stronger as a function of frequency and time. The  $a_{pha}$  parameter that represents the phase shift error in mrad for an impedance magnitude of  $|Z| = 1 \Omega$  was highest for the first measurement in dry soil. In addition,  $a_{pha}$ was found to systematically increase with frequency, particularly for frequencies above 10 Hz. This decrease in measurement accuracy is consistent with the findings of Kelter et al. (2015), who found an increase of the absolute error of the imaginary part of the complex electrical impedance data. The frequency dependency of the  $b_{pha}$  parameter that describes the decrease of the phase shift error with increasing impedance magnitude is much less pronounced. However, Figure 5 seems to suggest that this error parameter is somewhat higher for frequencies above 10 Hz. In addition, it was found that the  $b_{pha}$  parameter did not vary systematically between different measurement days. We hypothesize that these measurement errors are to some extent determined by the contact impedances of the non-polarizing electrodes. These contact impedances obviously depend on the bulk electrical conductivity of the subsurface, but are also determined by the fact that sponges used to make better contact with the soil were only rewetted periodically, and not before every EIT measurement. This possibly explained the less consistent changes observed for the  $b_{pha}$  parameter.

465

470

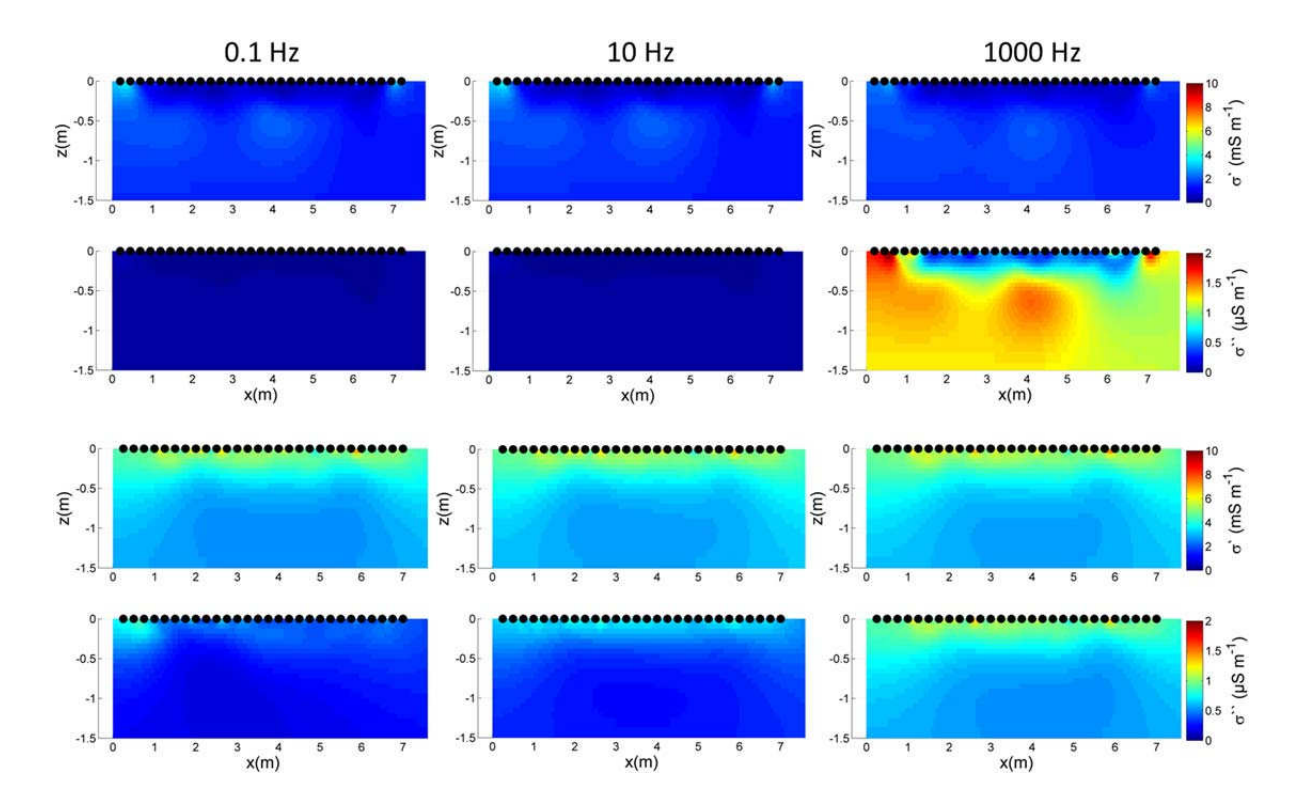


Figure 6. Inversion results for real and imaginary part of complex electrical conductivity at frequencies of 0.1 Hz (left), 10 Hz (center) and 1000 Hz (right) at day 0 (top two rows) and day 4 (bottom two rows).

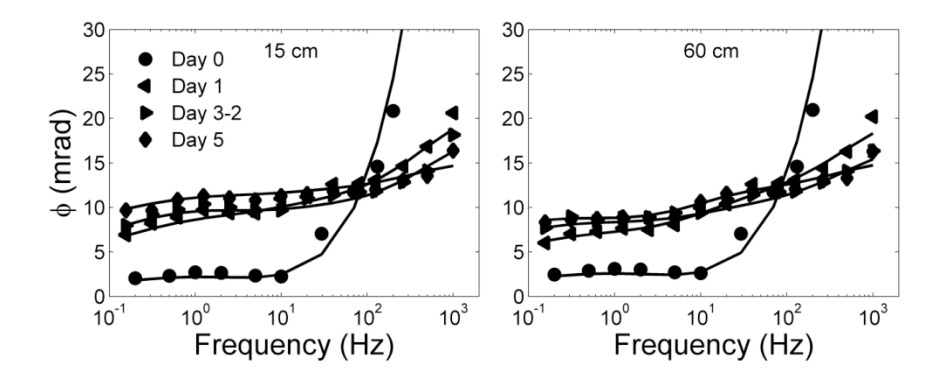
# 3.1.2 Spectral complex imaging results during the irrigation experiment

480

485

490

Figure 6 presents a compilation of inversion results for frequencies of 0.1 Hz, 10 Hz and 1000 Hz for two measurement days (before the irrigation at day 0 and day 4). The distribution of the real part of the electrical conductivity was homogeneous at day 0, as expected for a dry soil. After irrigation, the real part of the electrical conductivity increased, particularly for the top soil. As expected, the distribution of the real part of the electrical conductivity did not depend on the measurement frequency. In contrast, the imaginary part of the complex electrical conductivity consistently increased with frequency and the spatial distribution of the imaginary conductivity was consistent over the whole frequency range at both days. However, the increase of the imaginary conductivity deeper in the soil at day 0 in dry conditions seems erratic.



495 Figure 7. Inverted phase spectra of complex electrical conductivity, obtained for certain pixels at a lateral position of 3 m along the profile and depths of 20 cm (left) and 60 cm (right) for representative measurement dates. Solid lines illustrate the obtained Debye-decomposition fits.

Two representative pixels for the topsoil and subsoil layers were chosen at a depth of 15 cm and 60 cm and a lateral position of 3 m in order to illustrate the spectral variation of the complex electrical conductivity of individual pixels obtained from the inversion (Figure 7). These phase spectra of individual pixels show that the phase increased in response to irrigation in the low frequency range (< 10 Hz), whereas it decreased for the higher frequency part of the spectrum (i.e. > 10 Hz) except for the EIT measurements made at day 0 that seemed to behave differently. This is attributed to additional errors caused by capacitive coupling between the cable shield and soil (see Zhao et al., 2013) that become important when EIT measurements are made on soils with a low conductivity and high electrode contact impedances. Similar behavior was observed in Ghorbani et al. (2008) and Kelter et al. (2015) for sand-clay mixtures, and more work is required to improve the reliability of EIT measurements in these conditions.

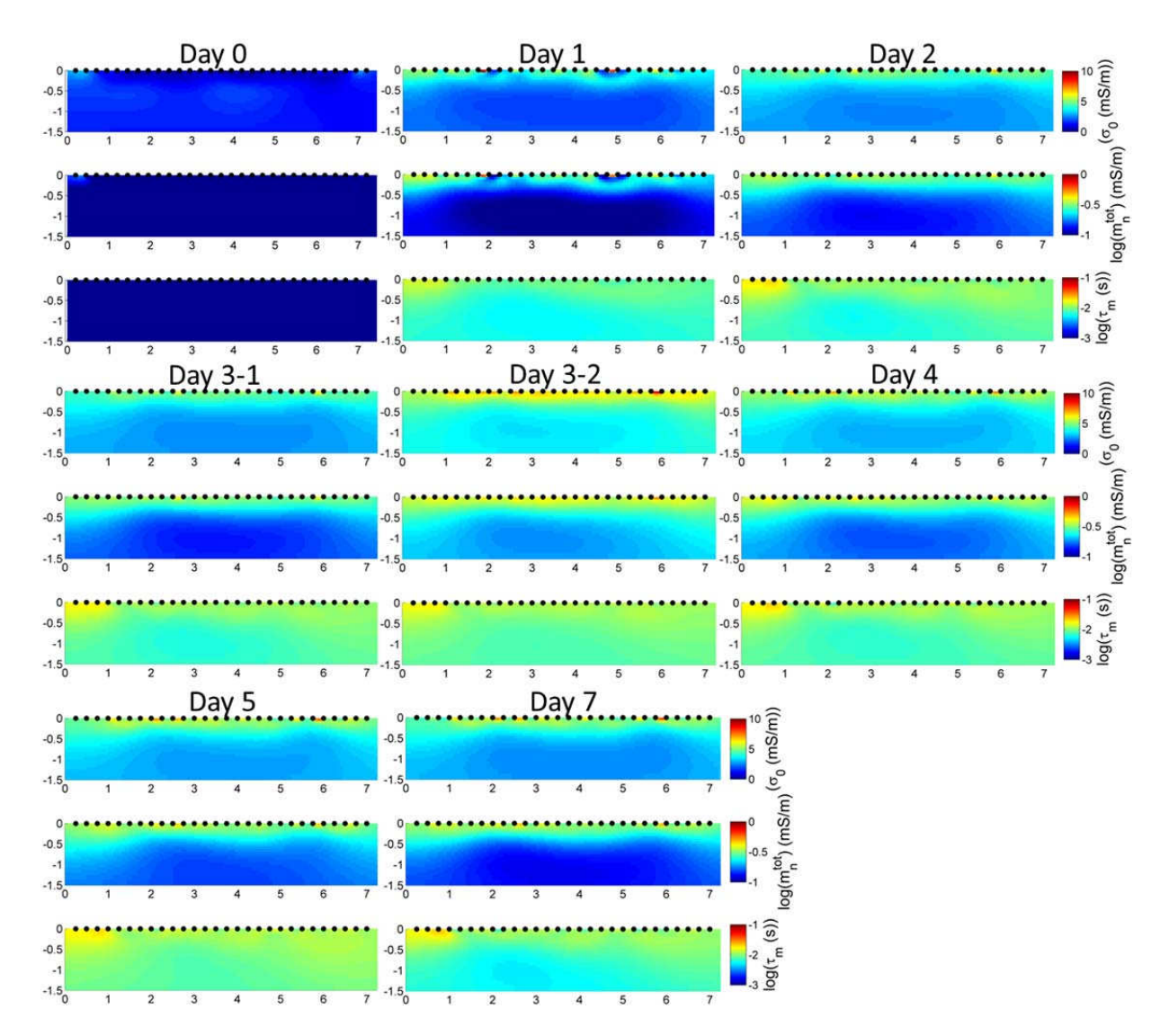


Figure 8. Spectral complex electrical inversion results in terms of DC-conductivity, normalized total chargeability and mean relaxation time, obtained by pixel-wise Debye-decomposition for all spectral electrical measurements during the irrigation experiment. Black dots indicate the positions of the electrodes.

520

The temporal development of the spatial distribution of integral spectral parameters obtained by Debye decomposition during the irrigation experiment is shown in Figure 8 and the good quality of the fit to the complex electrical conductivity of individual pixels is illustrated in Figure 7. It can be seen that the normalized total chargeability, the mean relaxation time, and the DC-electrical conductivity increased with increasing soil water content. The inversion

results suggest a two-layer structure, especially for the electrical conductivity and chargeability images. The results also indicate that changes in response to irrigation were much stronger in the top soil layer, and less pronounced deeper in the soil. This is attributed to the higher initial soil water content for the subsoil, as well as a much lower porosity. Independent TDR measurements indicated that the initial water content of the subsoil was about 0.15 cm<sup>3</sup>cm<sup>-3</sup>, whereas the estimated total porosity was 0.20 cm<sup>3</sup>cm<sup>-3</sup>.

525

540

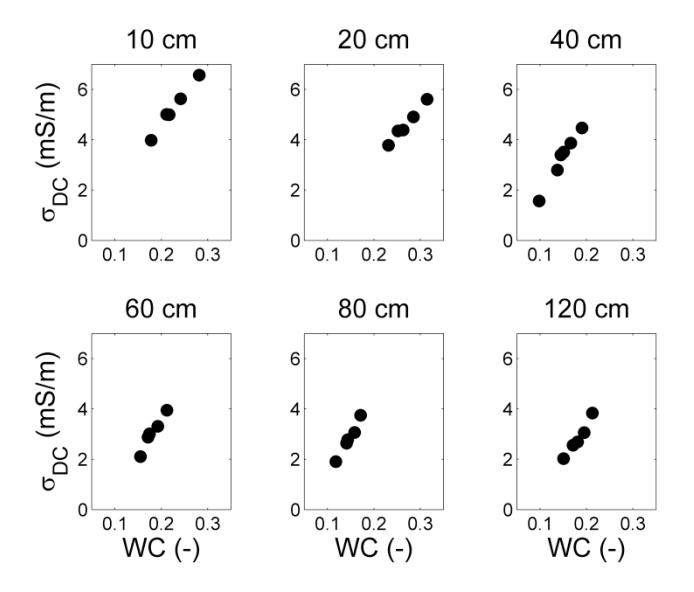


Figure 9. Mean DC electrical conductivity from x = 2 m to 6 m obtained from the inverted spectral electrical conductivity images plotted as a function of measured soil water content using TDR probes at a position of x = 0.75 m and the corresponding depths. Due to their erratic behaviour, measurements at day = 0 were not considered here.

# 535 *3.1.3 Relationships between water content and spectral electrical parameters*

The integral spectral parameters presented in Figure 8 were used to investigate relationships between spectral electrical properties and water content of the soil obtained from TDR. For this, the EIT inversion results at six depths were averaged from 2 to 6 m, which is justified given the limited lateral variation in the spectral electrical properties (Figure 8). Approximately linear relationships between the real part of the electrical conductivity and

water content were found for a limited range of water content (Figure 9). Similar linear relationships have been reported by Oberdörster et al. (2010) and Michot et al. (2003). The normalized total chargeability was also found to increase with water content (Figure 10). Only a few studies are available that have investigated the dependence of the normalized total chargeability on soil water content and they have reported different types of relationships. For example. Binley et al. (2005) observed decreasing phase shift values (and thus decreasing chargeability) with increasing water content for sandstone samples, whereas Grunat et al. (2013) reported increasing phase values with increasing water content for their soil sample. Breede et al. (2012) reported a more complex dependence of the normalized total chargeability on water content with increasing values in the low to medium saturation range and a rapid decrease of normalized total chargeability near full saturation. The results presented here are consistent with previously reported findings of Breede et al. (2012) and Grunat et al. (2013). Finally, we observed a slight but consistent increase in mean peak relaxation time with increasing saturation (Figure 11). This is also consistent with previous findings of Binley et al. (2005) and Breede et al. (2012), and this is typically explained by a decreasing characteristic polarization length scale with desaturation due to the decreasing size of the saturated pores.

545

550

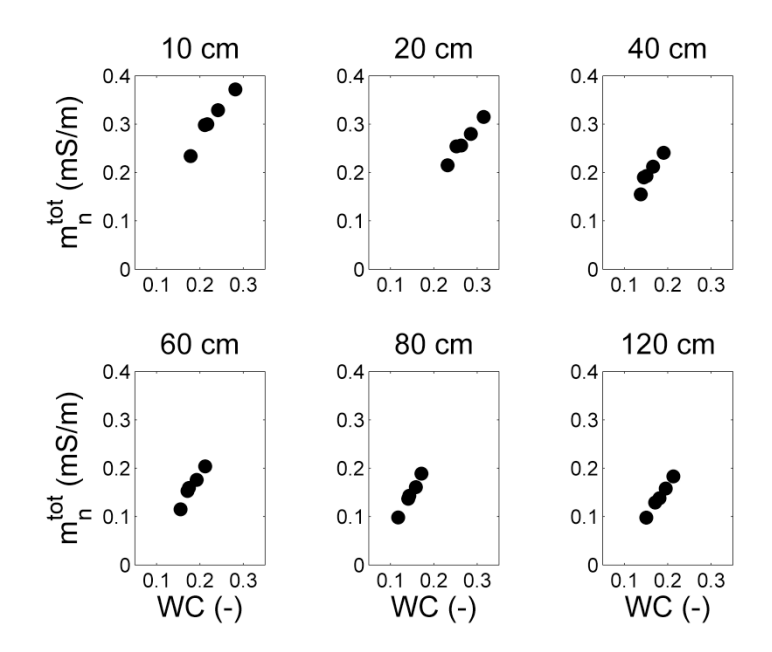


Figure 10. Mean normalized total chargeability from x = 2 m to 6 m obtained from the inverted spectral electrical conductivity images as a function of measured soil water content using TDR probes at a position of x = 0.75 m and the corresponding depths. Due to their erratic behaviour, measurements at day = 0 were not considered here.

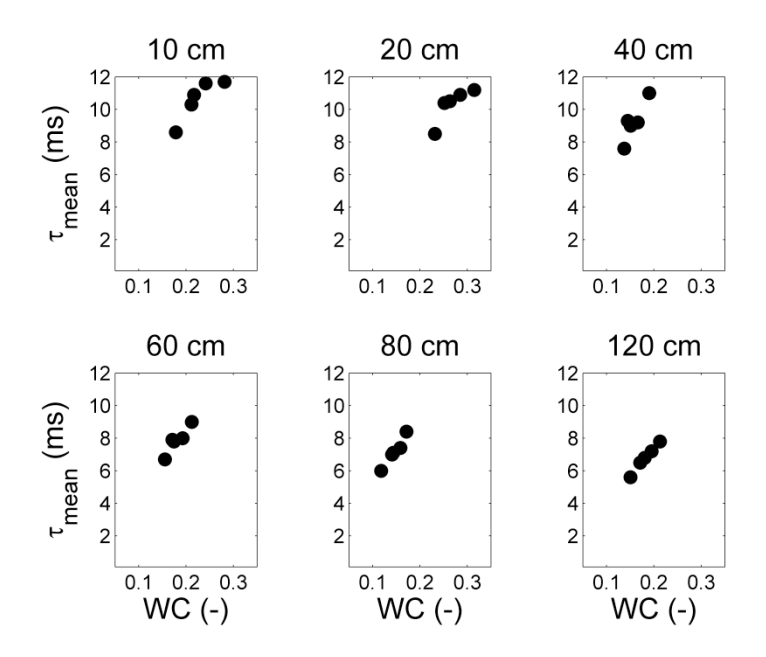


Figure 11. Mean relaxation time from x = 2 m to 6 m obtained from the inverted spectral electrical conductivity images as a function of measured soil water content using TDR probes at a position of x = 0.75 m and the corresponding depths. Due to their erratic behaviour, measurements at day = 0 were not considered here.

In general, Figures 9-11 also seem to indicate that the relationships between the spectral electrical parameters and water content were similar for all soil depths. However, the increase in DC-conductivity, normalized total chargeability, and mean relaxation time for a given change in water content decreases with depth. This is likely associated with the effects of the regularization, since the resolution of surface EIT measurements decreases significantly with depth. This is a general limitation of electrical imaging methods, and a detailed evaluation is beyond the scope of this study. In principle, the relationships shown in Figure 9-11 can be used to estimate water content distributions. If significant changes in the electrical conductivity of the pore water are expected, a relationship between water content and  $\sigma''$  or  $m_n^{tot}$  may be less affected than the bulk electrical conductivity and may thus be preferable (Grunat et al., 2013).

The spatial and spectral consistency of the results presented in this section clearly highlight that the processing and inversion strategy for laboratory EIT measurements developed in Kelter et al. (2015) also provides meaningful results for field EIT measurements where conditions are generally less favorable due to high and temporally variable electrode contact impedances. However, it seems that leakage currents due to capacitive coupling of the cables with the ground must be considered when electrode contact impedances are high due to a very dry top soil. This source of error is not (yet) well understood and requires further investigation. Of course, the EIT measurement set-up used here is only useful for small-scale field investigations because of the use of short cables to minimize the effect of inductive coupling between the cables (Zhao et al., 2015). In the next section, the robustness of the processing and inversion strategy is explored for borehole EIT measurements with long electrode chains.

#### 3.2 Borehole imaging in an unconfined aquifer

595

600

605

610

Borehole EIT measurements were performed using long multicore-cables that require the consideration of inductive coupling effects. However, since electrodes are galvanically coupled to the subsurface through the water-filled borehole, the electrode contact impedance is low and thus the key source of error in the surface EIT measurements presented earlier is not present here. Figure 12 shows the measurement error as a function of frequency obtained from normal and reciprocal measurements for borehole EIT measurements with and without correction for inductive coupling (after data filtering). It is important to note that the measurement error is not significantly affected by the correction for inductive coupling. This highlights that the effects of inductive coupling are reciprocal, which was already suggested by Zhao et al. (2015). This implies that errors due to inductive coupling cannot be corrected in an indirect manner through a higher error during inversion, and should thus be corrected a priori.

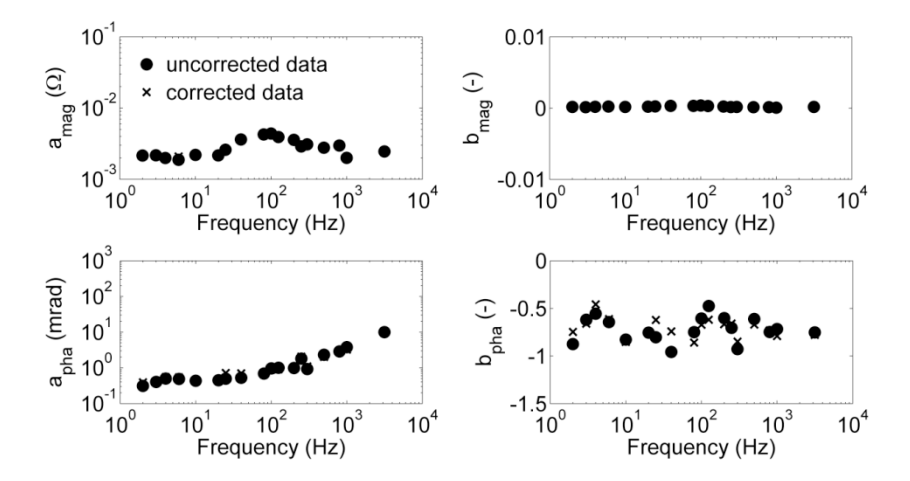


Figure 12. Error parameters for magnitude (top) and phase shift error (bottom) of uncorrected and corrected data as obtained by normal-reciprocal analysis for borehole EIT measurement data of the Krauthausen test site.

In general, the spectral behavior of the error parameters is similar to the results shown in Figure 5 for surface EIT measurements. Both the absolute  $(a_{mag})$  and the relative error

parameter (b<sub>mag</sub>) of the magnitude of the transfer impedances showed no frequency dependence. A small peak between 50 and 200 Hz in a<sub>mag</sub> indicates noise associated with power supply systems in the vicinity of the Krauthausen test site. The values a<sub>mag</sub> are difficult to compare between the two case studies because the range of measured impedances in the surface EIT measurements (1 Ω - 1 kΩ) was different from that in the borehole EIT measurements (0.01 Ω - 20 Ω). However, it can be observed that a<sub>mag</sub> was about two orders of magnitude higher in the irrigation experiment, which corresponds to the two order of magnitude difference in the measured ranges. The low values for b<sub>mag</sub> for the borehole EIT measurements are in good agreement with the results of the irrigation experiment, where this parameter only was significantly higher in dry conditions due to high electrode contact impedances.

A comparison of the error parameters of the phase shift in the two case studies shows a monotonic increase of the absolute error parameter  $(a_{pha})$  with frequency in both cases. Also the range of the observed values for  $a_{pha}$  matches very well between the two case studies. In the irrigation experiment, the relative error parameter  $(b_{pha})$  increased for frequencies above 10 Hz. Similar behavior was not observed in the borehole data (Figure 12). For the borehole data,  $b_{pha}$  ranged from -0.84 to -0.45, while it ranged from -0.80 to -0.02 in the irrigation experiment. The higher errors in the irrigation experiment are again attributed to the effect of the higher electrode contact impedances on the measurement accuracy.

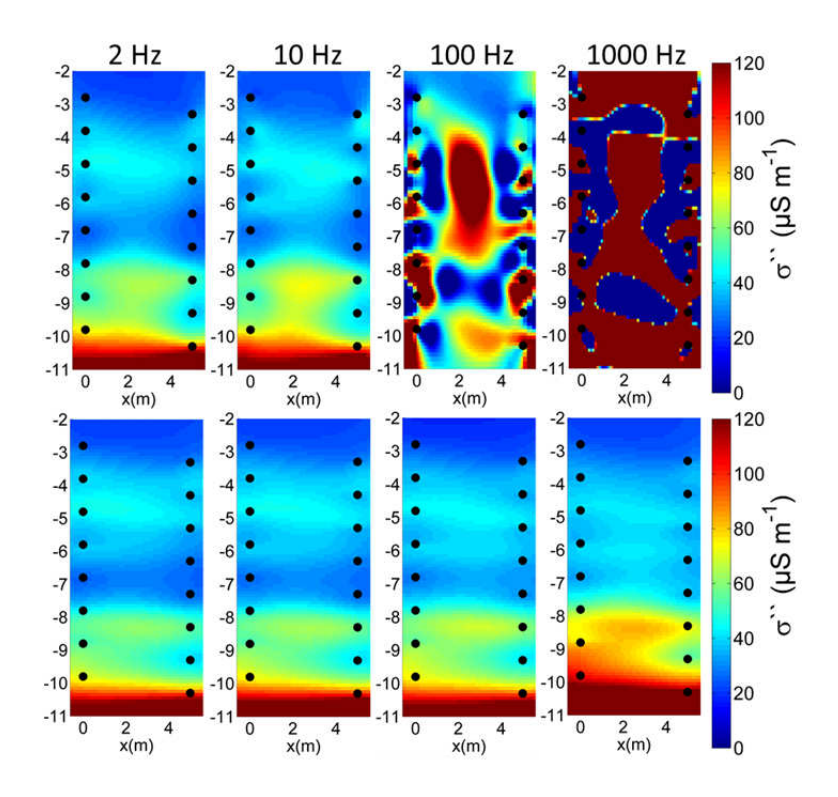


Figure 13. Imaging results for the imaginary part of complex electrical conductivity at frequencies of 2, 10, 100 and 1000 Hz for uncorrected (top) and corrected (bottom) data.

EIT imaging results for the imaginary conductivity at frequencies of 2, 10, 100 and 1000 Hz are shown in Figure 13 for data with (bottom) and without (top) corrections for inductive coupling. The distribution of the real part of the complex electrical conductivity was found to be independent of frequency (not shown). In the low frequency range (until 10 Hz), the inversion results for uncorrected and corrected data showed very similar results. For frequencies above 10 Hz, the inversion results for the uncorrected data showed increasingly strong artefacts whereas the corrected data resulted in EIT images that show the same structures that were present in the lower frequencies. Clearly, the correction for inductive coupling strongly increased the spectral consistency of the EIT imaging results. In some regions, there even was an increase in contrast at high frequencies, which indicates the added value of spectral information at higher frequencies.

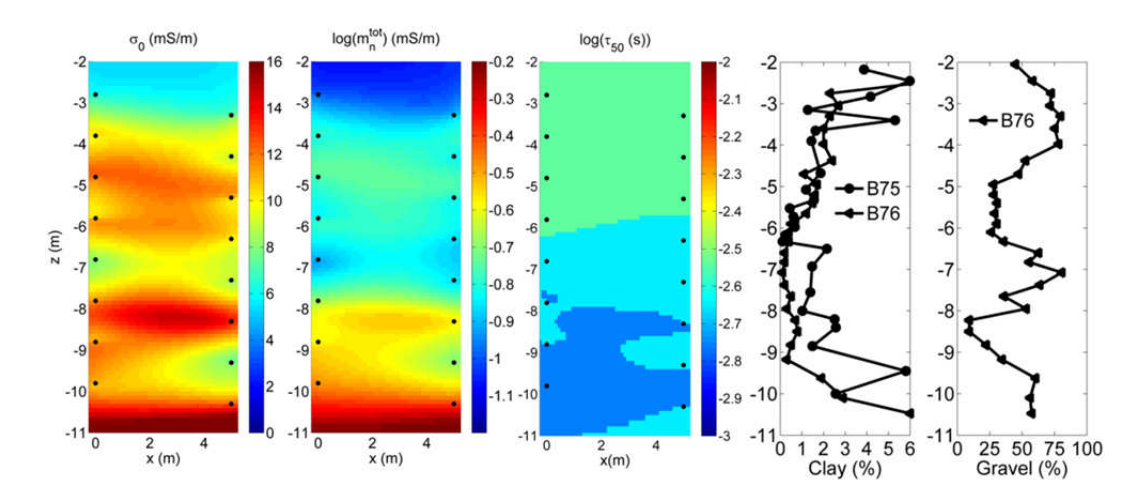


Figure 14. Integral spectral parameters obtained from spectral analysis of the imaging results for all individual frequencies for the corrected data. Parameters shown are DC-conductivity (left tomogram), normalized total chargeability (middle tomogram) and median relaxation time (right tomogram). The two panels on the right show profiles of the clay fraction (< 2  $\mu$ m) and gravel content (> 2mm) obtained for sediments from boreholes B75 and B76.

The imaging results for each frequency were again analyzed using the Debye decomposition approach. The three resulting integral spectral parameters DC-electrical conductivity, normalized total chargeability, and median relaxation time are shown in Figure 14. Layers with higher electrical conductivity were observed between 4 and 6 m depth, between 8 and 9 m depth, and below 10 m in the DC-conductivity image. The normalized total chargeability qualitatively showed the same results as the imaginary conductivity in Figure 13. However, the layer between 4 and 6 m depth was not as clear as for the DC conductivity, whereas the layers between 8 m and 9 m and below 11 m showed a stronger contrast when the normalized total chargeability was considered. The median relaxation time also showed the distinct layer between 8 and 9 m, as well as the general three-layer lithology of the aquifer at the Krauthausen site.

In order to validate the spectral electrical imaging results, they are compared to hydrological and sedimentological characteristics of the aquifer. During the time of the measurement, the groundwater table was known to be at around 3 m below ground surface, which was well captured in the imaging results by the lower DC-conductivity and normalized total chargeability. The more electrically conductive zones between 4 and 6 m and 8 and 9 m matched well with zones of higher porosities that are associated with a significantly lower gravel content (right panel of Figure 14). Furthermore, the polarizable layer between 8 and 9 m was associated with a local maximum in clay content in borehole B75 and a less pronounced increase in clay content in borehole B76 (Figure 14). Below 9 m, the clay content strongly increased due to the clay base of the aquifer and this explained the observed increase in the DC conductivity and the normalized total chargeability.

# 4 Summary and Conclusions

In this study, the capability of recent improvements in pre-processing and inversion strategies to improve the accuracy and spectral consistency of complex electrical conductivity distributions in the mHz to kHz frequency range obtained from field EIT measurements was evaluated using two case studies. The first case study consisted of a controlled irrigation experiment on an initially dry soil, which was monitored by spectral EIT measurements. A comparison of EIT measurements with stainless steel electrodes and non-polarizable electrodes showed that the use of non-polarizable electrodes provided more accurate measurement results in terms of data reciprocity. Error-weighted inversion was used to obtain EIT images from 0.1 Hz to 1 kHz, which were subsequently analyzed using a Debyedecomposition approach to obtain integral spectral electrical parameters (DC-conductivity, normalized total chargeability, and mean relaxation time). All three integral parameters increased linearly with water content, and were consistent with previous laboratory SIP investigations. Overall, it was concluded from the spatial and spectral consistency of the

inversion results that the inversion strategy for laboratory EIT measurements developed in Kelter et al. (2015) also provided meaningful results for field EIT measurements where conditions are generally less favorable due to high and temporally variable electrode contact impedances. It was also found that additional correction methods are required to make accurate EIT measurements for very dry soil conditions and high electrode contact impedances, which is likely due to significant capacitive coupling between the cable shield and the soil that has a strong impact on the EIT measurements in these dry conditions.

The second case study focused on borehole EIT measurements in an unconsolidated sand-gravel aquifer. Because of the use of long cables, corrections were made to account for inductive coupling. Spectral electrical imaging was performed in a frequency range from 2 Hz to 3.15 kHz and the results were again analyzed using a Debye-decomposition approach. Inversion results with and without corrections for inductive coupling showed that correction is essential to obtain spatially and spectrally consistent inversion results for frequencies above 10 Hz. A comparison of EIT imaging results with clay and gravel content independently determined on material collected from the boreholes showed a good agreement in terms of layering.

Overall, the results of this study clearly highlight that improved soil and aquifer characterization using broadband spectral electrical imaging is now possible using dedicated EIT equipment combined with appropriate data processing and consistent inversion procedures. To the best of our knowledge, this study is the first to provide plausible EIT inversion results for frequencies up to 1 kHz in a field application, and this opens up opportunities to monitor processes that are expected to affect the complex electrical conductivity in the Hz to kHz frequency range, such as the polarization associated with calcite precipitation used for soil stabilization (Wu et al., 2010), injected nanoparticles for

contaminated site remediation (Flores-Orozco et al., 2015), or the monitoring and characterization of plant root systems (Weigand and Kemna, 2017).

# Acknowledgements

We gratefully acknowledge the SFB/TR32 "Patterns in Soil-Vegetation-Atmosphere Systems: monitoring, modeling, and data assimilation", which is funded by the Deutsche Forschungsgemeinschaft (DFG) for financial support. This research was also supported by the project "4D Electrical Impedance Tomography" funded by the German Ministry of Education and Research (BMBF) in the framework of the R&D Program GEOTECHNOLOGIEN (Grant 03G0743B).

#### References

735

- Bairlein, K., Hördt, A., and Nordsiek, S. (2014). The influence on sample preparation on spectral induced polarization of unconsolidated sediments. Near Surface Geophysics, 12(5): 667-677.
- Bechtold, M., Vanderborght, J., Weihermüller, L., Herbst, M., Günther, T., Ippisch, O., and Vereecken, H. (2012). Upward transport in a three-dimensional heterogeneous laboratory soil under evaporation conditions. Vadose Zone Journal, 11(2), doi:10.2136/vzj2011.0066.
- Binley, A., Slater, L.D., Fukes, M., and Cassiani, G. (2005). Relationship between spectral induced polarization and hydraulic properties of saturated and unsaturated sandstone, Water Resources Research, 41: W12417, doi:10.1029/2005WR004202.
  - Börner, F.D., Schopper, J.R., and Weller, A. (1996). Evaluation of transport and storage properties in the soil and groundwater zone from induced polarization measurements, Geophysical Prospecting, 44: 583-601.
- 345 Breede, K., Kemna, A., Esser, O., Zimmermann, E., Vereecken, H., and Huisman, J.A. (2011).

  Joint setup for determining spectral induced polarization and hydraulic properties. Vadose
  Zone Journal, 10: 716-726.
  - Breede, K., Kemna, A., Esser, O., Zimmermann, E., Vereecken, H., and Huisman, J.A. (2012).

    Spectral induced polarization measurements on variably saturated sand-clay mixtures.

    Near Surface Geophysics, 10(6): 479-489.
  - Bücker, M., and Hördt, A. (2013). Analytical modelling of membrane polarization with explicit parametrization of pore radii and the electrical double layer. Geophysical Journal International, 194(2): 804-813.
- Cai, G., Vanderborght, J., Klotzsche, A., van der Kruk, J., Neumann, J., Hermes, N., and Vereecken, H. (2016). Construction of minirhizotron facilities for investigating root zone processes. Vadose Zone Journal, 15(9): doi:10.2136/vzj2016.05.0043.
  - Flores-Orozco, A., Williams, K.H., Long, P.E., Hubbard, S.S., and Kemna, A. (2011). Using

- complex resistivity imaging to infer biogeochemical processes associated with bioremediation of an uranium-contaminated aquifer. Journal of Geophysical Research, 116: G03001.
- Flores-Orozco, A., Kemna, A., and Zimmermann, E. (2012a). Data error quantification in spectral induced polarization imaging. Geophysics, 77: 227–237.

765

- Flores-Orozco, A., Kemna, A., Oberdörster, C, Zschornack, L, Leven, C., Dietrich, P., and Weiss, H. (2012b). Delineation of subsurface hydrocarbon contamination at a former hydrogenation plant using spectral induced polarization imaging, Journal of Contaminant Hydrology, 136–137:131-144.
- Flores-Orozco, A., Velimirovic, M., Tosco, T., Kemna, A., Sapion, H., Klaas, N., and Bastiaens, L.L. (2015). Monitoring the injection of microscale zero-valent iron particles for groundwater remediation by means of complex electrical conductivity imaging. Environmental Science and Technology, doi:10.1021/acs.est.5b00208.
- Ghorbani, A., Cosenza, P., Ruy, S., Doussan, C., Florsch, N. (2008). Non-invasive monitoring of water infiltration in a silty clay loam soil using Spectral Induced Polarization. Water Resources Research, 44(8): W08402.
- Grunat, D.A., Slater, L.D., and Wehrer, M. (2013). Complex electrical measurements on an undisturbed soil core: Evidence for improved estimation of saturation degree from imaginary conductivity. Vadose Zone Journal, 12(4), doi:10.2136/vzj2013.03.0059
  - Hördt, A., Blaschek, R., Kemna, A., and Zisser, N. (2007). Hydraulic conductivity estimation from induced polarisation data at the field scale the Krauthausen case history. Journal of Applied Geophysics, 62(1): 33-46.
- Huisman, J.A., Zimmermann, E., Esser, O., Haegel, F.-H., Treichel, A., and Vereecken, H.
   (2016). Evaluation of a correction procedure to remove electrode contact impedance effects from broadband SIP measurements. Journal of Applied Geophysics, 135: 466-473.
   Jackson, J.D. (1975). Classical Electrodynamics. Wiley: 176, 263.

- Kelter, M., Huisman, J.A., Zimmermann, E., Kemna, A., and Vereecken, H. (2015).

  Quantitative imaging of spectral electrical properties of variably saturated soil columns.

  Journal of Applied Geophysics, 123: 333-344.
  - Kemna, A. (2000). Tomographic inversion of complex resistivity theory and application. Ph.D. thesis, Ruhr-University of Bochum, Germany.
- Kemna, A., Binley, A., Ramirez, A., and Daily, W. (2000). Complex resistivity tomography for environmental applications. Chemical Engineering Journal, 77: 11-18.
  - Kemna, A., Binley, A., and Slater, L. (2004). Crosshole IP imaging for engineering and environmental applications, Geophysics, 69: 97-107.
  - Kemna, A., Binley, A., Cassiani, G., Niederleithinger, E., Revil, A., Slater, L., and Zimmermann, E. (2012). An overview of the spectral induced polarization method for near-surface applications. Near Surface Geophysics, 10(6): 453-468.

- Koestel, J., Kemna, A., Javaux, M., Binley, A., and Vereecken, H. (2008). Quantitative imaging of solute transport in an unsaturated and undisturbed soil monolith with 3-D ERT and TDR. Water Resources Research, 44(12), W12411.
- Leroy, P., Revil, A., Kemna, A., Cosenza, P., and Ghorbani, A. (2008). Complex conductivity of water-saturated packs of glass beads. Journal of Colloid and Interface Science, 321: 103-117.
  - Michot, D., Benderitter, Y., Dorigny, A., Nicoullaud, B., King, D., and Tabbagh, A. (2003). Spatial and temporal monitoring of soil water content with an irrigated corn crop cover using surface electrical resistivity tomography. Water Resources Research, 39(5): 1138.
- Müller, K., Vanderborght, J., Englert, A., Kemna, A., Huisman, J. A., Rings, J., and Vereecken, H. (2010). Imaging and characterization of solute transport during two tracer tests in a shallow aquifer using electrical resistivity tomography and multilevel groundwater samplers. Water Resources Research, 46(3): W03502.

- Nordsiek, S., and Weller, A. (2008). A new approach to fitting induced-polarization spectra,

  Geophysics, 73(6): 235-245.
  - Oberdörster, C., Vanderborght, J., Kemna, A., Vereecken, H. (2010). Investigating preferential flow processes in a forest soil using Time Domain Reflectometry and Electrical Resistivity Tomography. Vadose Zone Journal, 9(2): 350-361.
- Oldenburg, D.W., Li, Y.G. (1994). Inversion of induced polarization data. Geophysics, 59(9): 1327-1341.
  - Pelton, W.H., Ward, S.H., Hallof, P.G., Sill, W.R., and Nelson, P.H. (1978). Mineral discrimination and removal of inductive coupling with multifrequency IP. Geophysics, 43: 588-609.
- Revil, A., and Florsch, N. (2010). Determination of permeability from spectral induced polarization in granular media. Geophysical Journal International, 181: 1480-1498.
  - Revil, A., Karaoulis, M., Johnson, T., and Kemna, A. (2012). Review: Some low-frequency electrical methods for subsurface characterization and monitoring in hydrogeology. Hydrogeology Journal, 20(4): 617-658.
- Slater, L. (2007). Near surface electrical characterization of hydraulic conductivity: From petrophysical properties to aquifer geometries-A review. Surveys in Geophysics, 28: 169-197.
  - Tillmann, A., Englert, A., Nyari, Z., Fejes, I., Vanderborght, J., and Vereecken, H. (2008). Characterization of subsoil heterogeneity, estimation of grain size distribution and hydraulic conductivity at the Krauthausen test site using Cone Penetration Test. Journal of Contaminant Hydrology, 95(1-2): 57-75.

- Titov, K., Komarov, V., Tarasov, V., and Levitski, A. (2002). Theoretical and experimental study of time domain-induced polarization in water-saturated sands. Journal of Applied Geophysics, 50: 417–433.
- Titov, K., Kemna, A., Tarasov, A., and Vereecken, H. (2004). Induced polarization of

- unsaturated sands determined through time domain measurements. Vadose Zone Journal, 3: 1160-1168.
  - Ulrich, C., and Slater, L. (2004). Induced polarization measurements on unsaturated, unconsolidated sands. Geophysics, 69(3), 762-771.
- Vanderborght, J., Graf, A., Steenpass, C., Scharnagl, B., Prolingheuer, N., Herbst, M., H.J.

  Hendricks-Franssen, and Vereecken, H. (2010). Within-field variability of bare soil evaporation derived from Eddy Covariance measurements. Vadose Zone Journal, 9(4): 943-954.
  - Vereecken, H., Döring, U., Hardelauf, H., Jaekel, U., Hashagen, U., Neuendorf, O., Schwarze, H., and Seidemann, R. (2000). Analysis of solute transport in a heterogeneous aquifer: the Krauthausen field experiment. Journal of Contaminant Hydrology, 45(3): 329-358.

- Weigand, M., and Kemna, A. (2016). Debye decomposition of time-lapse spectral induced polarisation data. Computers & Geosciences, 86: 34-45.
- Weigand, M. and Kemna, A. (2017). Multi-frequency electrical impedance tomography as a non-invasive tool to characterize and monitor crop root systems. Biogeosciences, 14: 921-939.
  - Weller, A., Nordsiek, S., and Debschütz, W. (2010). Estimating permeability of sandstone samples by nuclear magnetic resonance and spectral-induced polarization. Geophysics, 75(6): 215-226.
- Williams, K.H., Kemna, A., Wilkins, M.J., Druhan, J., Arntzen, E., N'Guessan, A.L., and Banfield, J.F. (2009). Geophysical monitoring of coupled microbial and geochemical processes during stimulated subsurface bioremediation. Environmental Science and Technology, 43(17): 6717-6723.
- Wu, Y., Hubbard, S., Williams, K.H., and Ajo-Franklin, J. (2010). On the complex conductivity signatures of calcite precipitation. Journal of Geophysical Research, 115:

G00G04.

865

- Zhao, Y., Zimmermann, E., Huisman, J.A., Treichel, A., Wolters, B., van Waasen, S., and Kemna, A. (2013). Broadband EIT borehole measurements with high phase accuracy using numerical corrections of electromagnetic coupling effects. Measurement Science and Technology, 24(8): 085005.
  - Zhao, Y., Zimmermann, E., Huisman, J.A., Treichel, A., Wolters, B., van Waasen, S., and Kemna, A. (2015). Phase correction of electromagnetic coupling effects in cross-borehole EIT measurements. Measurement Science and Technology, 26(1): 015801.
- Zimmermann, E., Kemna, A., Berwix, J., Glaas, W., and Vereecken, H. (2008a). EIT measurement system with high phase accuracy for the imaging of spectral induced polarization properties of soils and sediments. Measurement Science and Technology, 19: 094010.
  - Zimmermann, E., Kemna, A., Berwix, J., Glaas, W., Münch, H.-M., and Huisman, J.A. (2008b). A high-accuracy impedance spectrometer for measuring sediments with low polarizability. Measurement Science and Technology, 19: 105603.
  - Zisser, N., Kemna, A., and Nover, G. (2010). Relationship between low-frequency electrical properties and hydraulic permeability of low-permeability sandstones. Geophysics, 75: 131-141.